Highly monodisperse core–shell particles created by solid-state reactions

V. Radmilovic[1,2]*, C. Ophus[1], E. A. Marquis[3], M. D. Rossell[1,4], A. Tolley[1,5], A. Gautam[1], M. Asta[1,6] and U. Dahmen[1]

The size distribution of particles, which is essential for many properties of nanomaterials, is equally important for the mechanical behaviour of the class of alloys whose strength derives from a dispersion of nanoscale precipitates. However, particle size distributions formed by solid-state precipitation are generally not well controlled. Here we demonstrate, through the example of core–shell precipitates in Al–Sc–Li alloys, an approach to forming highly monodisperse particle size distributions by simple solid-state reactions. The approach involves the use of a two-step heat treatment, whereby the core formed at high temperature provides a template for growth of the shell at lower temperature. If the core is allowed to grow to a sufficient size, the shell develops in a 'size focusing' regime, where smaller particles grow faster than larger ones. These results suggest strategies for manipulating precipitate size distributions in similar systems through simple variations in thermal treatments.

Since the invention of dispersion-hardened Al alloys more than a century ago[1], the formation of second-phase particles by solid-state precipitation reactions has been used as a major strengthening mechanism for structural materials. The strong effects on mechanical properties arising from the formation of second-phase particles are well known, and exploited in applications ranging from energy generation to aerospace structures[2]. To fully optimize the properties of precipitation-strengthened alloys requires a detailed understanding of the factors controlling precipitate size, shape and thermal stability. Over the past decade, there has been significant progress in our understanding of these factors, mainly because of recent advances in atomic-scale characterization techniques such as aberration-corrected transmission electron microscopy (TEM) and atom-probe tomography (APT), coupled with the development of predictive atomic-scale modelling techniques[3–8]. In these studies new insights have been gained into the role of diffusion kinetics, capillarity and thermodynamic driving forces in governing particle morphologies, size distributions and coarsening kinetics.

In the present work we undertake a combined experimental and theoretical study of an AlLiSc alloy that forms novel core–shell precipitates[9–13]. Sc is the most potent strengthener for Al of all the elements in the periodic table; Li is the lightest metal; and both form Al_3X type intermetallic phases with a relatively simple $L1_2$ crystal structure that can grow as Al_3Sc stable[14] or Al_3Li metastable[15,16] coherent precipitates in the face-centred cubic (fcc) Al matrix. Thus, adding both Sc and Li to Al offers great potential for a lightweight alloy with high strength and stiffness. Previous investigations of core–shell precipitates in AlLiSc alloys have elucidated their structure, morphology and composition, and demonstrated highly monodisperse particle size distributions (PSD; refs 9–13). In this study we examine AlLiSc precipitation in detail and construct a kinetic model that explains the mechanisms underlying the exceptionally narrow PSD.

A two-stage ageing treatment used to induce solid-state precipitation leads to the distribution of $Al_3(Li, Sc)$ precipitates illustrated in Fig. 1a. The particles consist of a core of the Al_3Sc phase, which forms during a high-temperature annealing step (18 h at 450 °C), surrounded by a shell of Al_3Li, which forms during a subsequent lower-temperature heat treatment (4 h at 190 °C). From micrographs such as that shown in Fig. 1a we measured the size distributions plotted in Fig. 1b. The mean core radius, shell thickness and overall precipitate radius were found to be 9.2, 10.5 and 19.8 nm respectively. To estimate the width of the size distribution, the full-width at half-maximum (FWHM) w was measured from best-fit skew normal distributions. The size ranges were found to be unusually tight, with values (given in terms of their fraction of the mean radius or thickness $\bar{r}$) of $w/\bar{r} = 0.24$, 0.24 and 0.16 for the core radius, shell thickness and particle radius respectively. Such narrow size distributions are rare in solid-state precipitation systems, but are comparable to those formed in colloidal chemistry[17]. For comparison the size distribution of precipitates in a binary AlSc alloy that is typical of other Al-based alloys[18–21] is also plotted in Fig. 1b. This distribution has a fractional width $w/\bar{r} = 0.72$, which is 4.5 times the width of the AlLiSc overall PSD.

An important feature of the AlLiSc size distributions shown in Fig. 1b is the fact that the thickness of the core and shell are anti-correlated, such that the size distribution of the total core–shell particle is narrower than that of either the core or the shell. This feature provides important clues to the mechanisms underlying the formation of the narrow PSD, as will be explained below.

Before analysing the mechanisms controlling the PSD, we describe important features of the composition and structure of the particles. High-resolution TEM imaging of individual particles in a ⟨001⟩ zone axis orientation shows the core–shell structure in detail. As shown in Fig. 2, both the core and the shell are fully ordered in the $L1_2$ structure and fully coherent with the surrounding

[1]National Center for Electron Microscopy, Materials Science Division, Lawrence Berkeley National Lab, Berkeley, California 94720, USA, [2]Nanotechnology and Functional Materials Center, Faculty of Technology and Metallurgy, University of Belgrade, 11000 Belgrade, Serbia, [3]Department of Materials Science and Engineering, University of Michigan, Ann Arbor, Michigan 48109-2136, USA, [4]Department of Materials, ETH Zürich, 8093 Zürich, Switzerland, [5]Comisión Nacional de Energía Atómica, San Carlos de Bariloche, R8402AGP Río Negro, Argentina, [6]Department of Materials Science and Engineering, University of California, Berkeley, California 94720, USA. *e-mail: VRRadmilovic@lbl.gov; VRRadmilovic@tmf.bg.ac.rs.
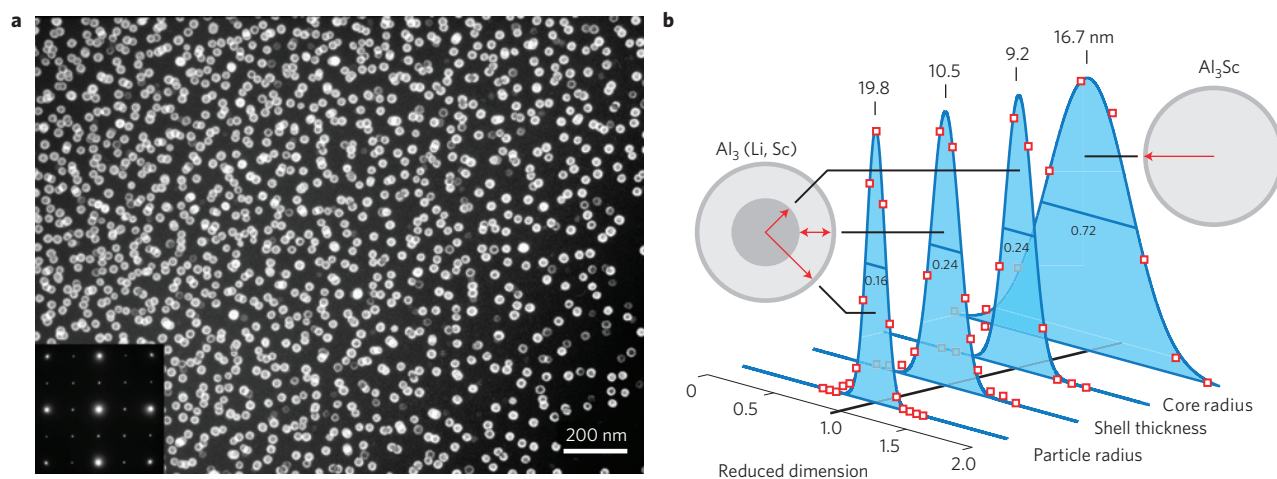
Figure 1 | Size distributions of precipitates in AlLiSc alloy measured with TEM. a, Dark field micrograph of an AlLiSc alloy, showing a remarkably uniform distribution of core–shell precipitates with $L1_2$ structure. The selected area diffraction pattern inset shows strong fcc reflections and weaker $L1_2$ superlattice reflections in a square pattern typical of an $\langle 001 \rangle$ crystal orientation. **b,** Particle size distributions comparing core, shell and core–shell sizes in the present alloy with the much broader distribution of a typical AlSc binary alloy. FWHM divided by mean shown on each distribution.
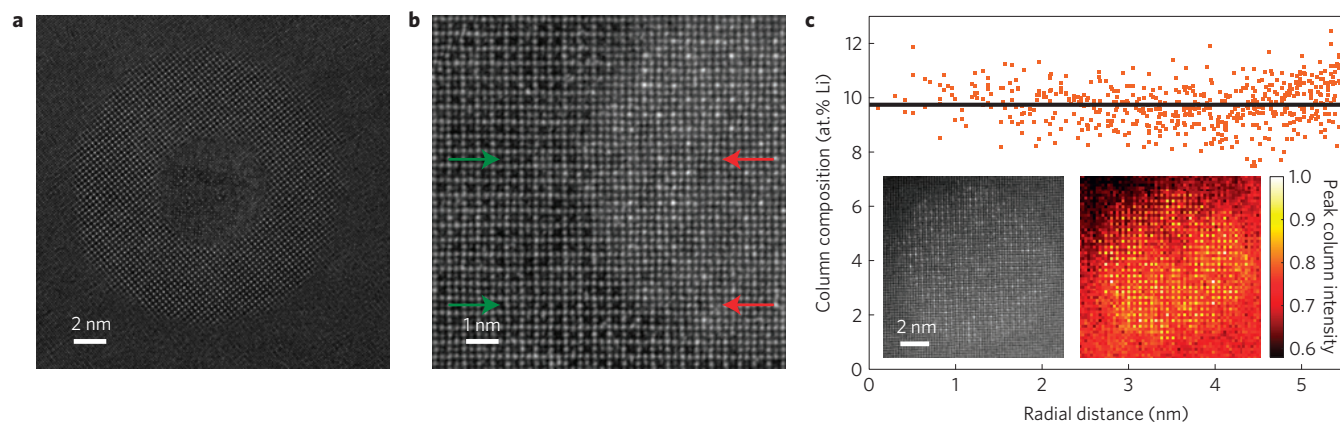

Figure 2 | Characterization of a single Al_3(Li, Sc) core–shell precipitate in Al. a, High resolution TEM micrograph. **b,** HAADF image of the core–shell interface; arrows show perfect alignment of the (Sc, Li) sublattice (red arrows) in the core with the Li sublattice (green arrows) in the shell. **c,** Li composition in atomic columns obtained from intensity measurements normalized to the local neighbourhood of the Al sublattice in the core region.

fcc matrix. There are no dislocations at the interface between the core and the shell, nor between the shell and the matrix. Based on energy-filtered TEM imaging and previously published APT analysis[13], we have concluded that the shell is nearly stoichiometric Al_3Li whereas the core is Al_3(Sc, Li), incorporating both Sc and Li on the B-site sublattice of the $L1_2$ A_3B structure. Using high-angle annular dark field (HAADF) scanning transmission electron microscopy (STEM) imaging, we found that the majority (Al) sublattice in the core phase exhibits very uniform contrast, indicating that these sites are occupied entirely by Al, with a negligible fraction of solute atoms. By contrast, the minority (Sc, Li) sublattice columns in the particle core show strong contrast variations, indicating mixing of Li and Sc on these sites. This contrast difference is also apparent from the enlarged view of the interface between the core and the shell shown in the HAADF image in Fig. 2b. The regularly ordered structure of the shell is clearly different from the more disordered structure of the core. Note, however, that this disorder is confined entirely to the minority (Sc, Li) sublattice and that this sublattice is in perfect alignment with the Li sublattice in the shell (see arrows).

An independent measure of the Li concentration in the core was obtained from HAADF STEM imaging of precipitate cores after the high-temperature step, but before the growth of the Li-rich shell

in the low-temperature step, Fig. 2c. Using an analysis technique that normalizes the signal from the $L1_2$ superlattice columns to the immediately adjacent pure Al columns, the composition of each column can be determined individually. As seen in the plot of the angularly-averaged concentration versus radius in Fig. 2c, the composition of 9.7 ± 2.4 at.% Li is uniform across the entire core. This composition is very close to that obtained with APT analyses (see Supplementary Informations and ref. 13) for the Li concentration in the cores after the second, lower-temperature annealing step. The results thus show that the composition of the core does not change appreciably during the second heat treatment. These conclusions were also confirmed by energy-filtered TEM imaging using the composition-dependent shift of the plasmon peak. The measurements reported here and in[11–13] all agree in showing appreciable incorporation of Li in the core of the precipitates.

To understand the mechanisms underlying the formation of the narrow size distributions reported in Fig. 1b, we have undertaken an analysis of the nucleation and growth rates within the framework of the mean-field kinetic theory developed by Kuehmann and Voorhees (KV; ref. 22). In this formalism, particles grow or shrink at a rate determined by solute diffusion in the matrix phase, subject to constraints imposed by capillary-corrected local chemical equilibrium at the matrix/particle interface, mass conservation,
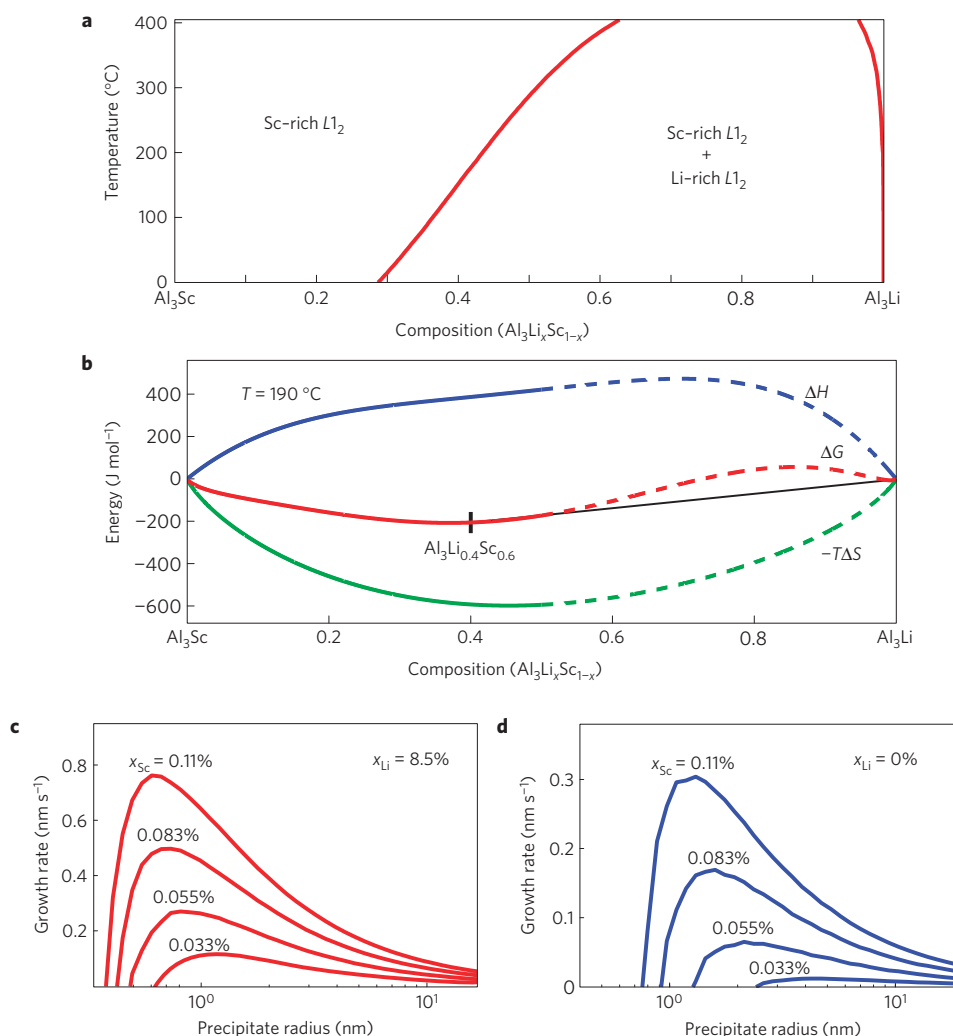
Figure 3 | Thermodynamic and kinetic modelling of Al$_3$(Li, Sc) precipitation. a, Calculated phase diagram of Al$_3$Sc–Al$_3$Li pseudo-binary system and **b**, energies at 190 °C. **c,d**, Growth kinetics of Al$_3$(Li, Sc) (**c**) and Al$_3$Sc (**d**) plotted as a function of precipitate radius and matrix Sc solute concentration. x_{Li} and x_{Sc} refer to the matrix solute concentrations.

and the value of the far-field solute compositions. As described in detail in the Supplementary Information, the application of the KV formalism to the present system makes use of previously published measurements of the Sc and Li diffusion coefficients in the Al matrix[23,24], interfacial free energies[25,26], and a thermodynamic model combining published free-energy parameterizations for the binary Al–Sc (ref. 27) and Al–Li (ref. 28) systems with a mixing free energy for the Al$_3$Li − Al$_3$Sc L1$_2$ phase derived from first-principles-based Monte Carlo simulations.

An important feature of the thermodynamic properties underlying particle formation is reflected in the Monte Carlo-calculated phase diagram of the Al$_3$(Li$_x$Sc$_{1-x}$) pseudobinary system shown in Fig. 3. A wide miscibility gap exists between the Sc-rich and the Li-rich L1$_2$ phases. The gap is highly asymmetric, with a much higher solubility for Li in Al$_3$Sc than for Sc in Al$_3$Li. At 190 °C, the stable phases predicted are Al$_3$Li$_{0.4}$Sc$_{0.6}$ and Al$_3$Li, very close to the compositional measurements described above for the precipitate core and shell using APT and STEM. The core–shell precipitates in the investigated AlLiSc alloy are therefore predicted to be thermodynamically stable phases, with no driving force for the diffusion of Li out of the core into the shell.

We now examine the formation of the core phase during the first-step heat treatment at high temperature. Using the thermodynamic models described above, and published interfacial

energies, we predict that the addition of Li to the binary AlSc system will decrease the energy barrier to nucleation and cause a considerable acceleration of the nucleation rate of Al$_3$Sc, by roughly five orders of magnitude. This effect reflects a prediction that the presence of Li lowers the solubility of Sc in Al, which elevates the supersaturation of Sc and thus increases the driving force for nucleation. In addition, as shown in Fig. 3b, Li also has a pronounced effect on the growth rates of the Sc-rich precipitate cores. The curves in Fig. 3b represent the calculated growth rates (dr/dt) versus particle radius (r), and feature an initial rise with particle size, reflecting capillary effects, a maximum, and a subsequent monotonic decrease. The calculations show that Li incorporation into the core leads to higher growth rates overall (because the system is kinetically limited by the Sc diffusion). Furthermore, Li also lowers the critical radius (for which dr/dt = 0) for all solute concentration levels. During the high-temperature heat treatment, these factors lead to a burst of nucleation followed by rapid depletion of Sc solute. It is worthwhile pointing out, however, that the narrow PSD for the cores inherited from the high-temperature anneal would be expected ultimately to broaden if the annealing time was extended long enough for the kinetics to enter the usual coarsening regime. Hence, key to the narrow PSD for the core is to limit the high-temperature annealing time to avoid this coarsening regime.
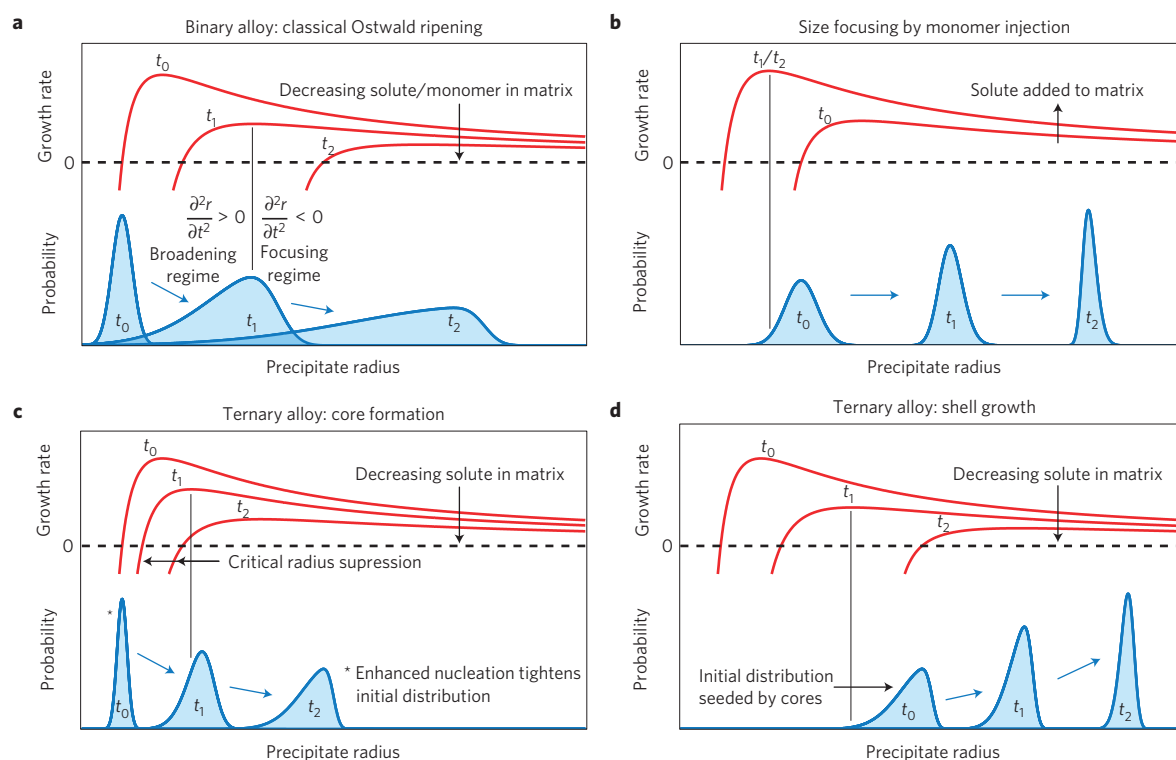
Figure 4 | Comparison of the evolution of precipitate sizes using the method described in this study with classical Ostwald ripening and an alternate route used in colloid synthesis. Precipitate growth rates and size distributions as a function of size are shown for three time steps for **a**, classical Ostwald ripening in a typical binary alloy, **b**, size focusing in a colloidal solution using solute injection[17], **c**, core formation and **d**, shell growth used in this study. The vertical divider line separates the broadening from the focusing regime for time t_1.

We consider next the evolution of the shell phase during the second-step heat treatment at low temperature, where the very large difference in diffusion rates between Sc and Li essentially renders the Sc immobile. This effectively turns the Al$_3$Sc precipitate cores into inert spherical substrates for the solid-state epitaxial growth of Al$_3$Li. First-principles calculations of the excess energies (γ) for the relevant interfaces show that $\gamma(\mathrm{Al}/\mathrm{Al_3Sc}) > \gamma(\mathrm{Al}/\mathrm{Al_3Li}) + \gamma(\mathrm{Al_3Li}/\mathrm{Al_3Sc})$ (ref. 29). Thus, the Al$_3$Li shell can form on the Al$_3$Sc core through a 'barrier-less' process of solid-state wetting, without the need for further nucleation. As the size distribution of the precipitates is inherited from the previously grown cores, the average radius of curvature of the shell/matrix interface is predicted to be well beyond the maximum in the growth-rate versus size curves calculated by the KV model at this temperature. In other words, the radius of curvature of the matrix/shell interfaces inherited from their core 'templates' is sufficiently large to place all particles on the downward slope of the calculated curve of $\mathrm{d}r/\mathrm{d}t$ versus r. Thus, smaller particles will grow more quickly than larger particles, leading to a narrowing of the size distribution. This explains why the size distributions of the core and the shell are anti-correlated, and the overall size distribution of the core–shell precipitates is narrower than that for the cores shown in Fig. 1b. We note that in certain cases elastic interactions between precipitates and the matrix can also lead to narrowing of the precipitate size distribution[30]; however, this mechanism can be ruled out for AlLiSc because of the small elastic strain between Al and both Al$_3$Li (ref. 16) and Al$_3$Sc (ref. 14).

The model outlined above suggests that creation of highly monodisperse precipitates is subject to both compositional and thermal constraints. To drive the nucleation burst of Sc-rich cores, the Li concentration should be as high as possible yet still low enough to prevent the stable AlLi precipitates from forming during the shell-growth stage. The core must be grown at a high enough

temperature to prevent the formation of isolated Al$_3$Li precipitates, and for a short enough time to prevent appreciable coarsening. Finally, the supersaturation of Li at the lower annealing temperature needs to be large enough for the maximum in the growth rate curve to lie below the size of the core particles.

To further illustrate our model of the processes underlying the narrowing of the precipitate size distribution, Fig. 4 shows schematic curves of growth rates as a function of size, along with snapshots of the size distribution for three different hypothetical time steps during the isothermal annealing, t_0, t_1 and t_2. If the precipitate sizes are larger than the critical radius, corresponding to the crest in the growth rate curves indicated by a vertical divider line for time t_1, the growth is said to be in the narrowing, or 'size-focusing', regime. In this regime the small precipitates grow at a faster rate than the larger ones, leading to a narrowing of the size distribution. Such behaviour can be contrasted with the more normal case of classical Ostwald ripening outlined in Fig. 4a. In this case, smaller particles shrink and larger particles grow, leading to a broadening of the size distribution with time.

As an approach to the growth of monodisperse particles, the mechanism described above shares features in common with the well-established LaMer model, which separates the nucleation and growth stages in the formation of monodisperse particles from colloidal solution[31]. The strategy used to create monodisperse particles in colloidal synthesis is illustrated in Fig. 4b. In this approach, precipitates are initially nucleated at a low monomer (solute) concentration. After nucleation, an injection of monomer into the system reduces the critical radius and pushes the PSD into the focusing regime. The two-step process operating in the Al–Sc–Li alloy is illustrated in Fig. 4c,d. During the initial heat treatment (Fig. 4c), the alloy addition of Li serves to greatly increase the nucleation rate of Sc-rich precipitates, which thus begin with a narrower distribution relative to the binary Al–Sc

system. Li also suppresses the increase of critical radius with decreasing amounts of Sc solute, which keeps the distribution from widening too much. The subsequent low-temperature heat treatment (Fig. 4d) begins with Al_3Li wetting the surface of the precipitate cores previously grown. As the precipitate size distribution starts at a mean radius of 9 nm it is firmly in the focusing regime and becomes narrower as the wetting layer grows to become an Al_3Li shell.

The mechanisms elucidated above are anticipated to offer unique opportunities for controlling PSD in related alloy systems. For example, it is expected that the formation of narrow size distributions will lead to a considerable delay in the onset of particle coarsening. Significant particle coarsening will commence only when the solute concentration in the matrix is reduced to the point that the critical radius reaches values very close to the average particle size. This reduction of the coarsening rate offers a strategy for designing microstructures with increased stability at higher temperatures. Another interesting possibility arises in exploiting the mechanisms described above to develop bimodal size distributions. Specifically, we have found that in samples where the second ageing treatment is extended to very long times, a bimodal distribution arises with a peak at larger r corresponding to particles with large shells, and a peak at small r corresponding to precipitates with a thin layer of the shell phase wetting the core. This would occur when the critical radius of the Al_3Li shell becomes larger than some of the particle cores, driven by near-total depletion of Li in the matrix. Further work is warranted to understand the late-time dynamics of the precipitate microstructures in this system, and to explore the interesting consequences that such bimodal PSD may have on the mechanical properties of these alloys.

We end by speculating that the phenomena described in this article are expected to be observable in other core–shell systems. The key ingredients for the method described in this work are to form a core phase with a relatively narrow size distribution in a burst of nucleation and to grow the core phase sufficiently to place it in the 'size focusing' regime during the subsequent shell growth. Core–shell precipitates have been observed in a number of alloy systems (for example, ref. 32, and references therein), and the mechanisms elucidated here offer an opportunity to control their size and distributions at a level that has so far has not been possible to achieve.

Methods

Alloy preparation. The AlLiSc alloy used in this study contained 8.46 at.% Li and 0.11 at.% Sc, as well as a 0.02 at.% Zr impurity. The samples were produced in a ~15 torr argon atmosphere in an electric arc furnace, followed by quenching in a water-cooled Cu mold. Three subsequent heat treatments were employed: homogenization for 72 h at 640 °C, annealing for 18 h at 450 °C (stage 1) and ageing for 4 h at 190 °C (stage 2). Each treatment was performed inside a sealed quartz tube filled with argon.

Transmission electron microscopy. Electropolished TEM samples were imaged at 80 and 300 kV on the TEAM 0.5 aberration-corrected microscope at the National Center for Electron Microscopy.

First-principles calculations. First-principles calculations were performed within the framework of electronic density functional theory, employing the Perdew–Burke–Ernzerhof generalized-gradient approximation[33] and the projector augmented wave (PAW) formalism[34,35], as implemented in the Vienna *ab initio* simulation program (VASP; refs 36–38). We employed the Al, Sc and Li PAW potentials labelled 'Al,' 'Li_sv' and 'Sc_sv' in the VASP library, a plane-wave cutoff of 400 eV, and a sufficient density of k-points to converge the energy of the intermetallic compounds to within approximately 1 meV/atom. To compute the mixing free energies for $Al_3(Li_xSc_{1-x})$ compounds we employed the cluster expansion formalism, using the algorithms included in the Alloy Theoretic Automated Toolkit (ATAT) package developed by van de Walle and co-workers[39]. The cluster expansion for the $Al_3(Li_xSc_{1-x})$ pseudobinary system made use of VASP-calculated energies for 89 structures, which were fit using 11 pair, 28 triplet and 11 four-body cluster interactions, giving a cross-validation score of 1.39 meV/atom.

References

1. Gayle, F. & Goodway, M. Precipitation hardening in the first aerospace aluminum-alloy—the Wright Flyer crankcase. *Science* **266,** 1015–1017 (1994).
2. Lu, K. The future of metals. *Science* **328,** 319–320 (2010).
3. Mao, Z., Sudbrack, C. K., Yoon, K. E., Martin, G. & Seidman, D. N. The mechanism of morphogenesis in a phase-separating concentrated multicomponent alloy. *Nature Mater.* **6,** 210–216 (2007).
4. Clouet, E. *et al.* Complex precipitation pathways in multicomponent alloys. *Nature Mater.* **5,** 482–488 (2006).
5. Sigli, C. *Aluminium Alloys: Their Physical and Mechanical Properties* 50–59 (Wiley–VCH, 2008).
6. Ardell, A. & Ozolins, V. Trans-interface diffusion-controlled coarsening. *Nature Mater.* **4,** 309–316 (2005).
7. Srinivasan, R. *et al.* Atomic scale structure and chemical composition across order–disorder interfaces. *Phys. Rev. Lett.* **102,** 86101 (2009).
8. Marquis, E. A., Seidman, D. N., Asta, M., Woodward, C. & Ozolins, V. Mg segregation at Al/Al_3Sc heterophase interfaces on an atomic scale: Experiments and computations. *Phys. Rev. Lett.* **91,** 036101 (2003).
9. Miura, Y., Horikawa, K., Yamada, K. & Nakayama, M. in *Aluminum Alloys: Their Physical and Mechanical Properties, Papers Presented at the International Conference, 4th, Atlanta, Sept. 11–16, 1994 (1994),* Vol. 2 (eds Sanders, T. H. & Starke, E. A.) 161–168 (Georgia Institute of Technology, 1994).
10. Berezina, A. L., Kolobnev, N. I., Chuistov, K. V., Kotko, A. B. & Molebny, O. A. Coherent composite phases formation in aged Al–Li base alloys. *Mater. Sci. Forum* **396–402,** 977–982 (2002).
11. Krug, M. E., Dunand, D. C. & Seidman, D. N. Composition profiles within Al_3Li and Al_3Sc/Al_3Li nanoscale precipitates in aluminum. *Appl. Phys. Lett.* **92,** 124107 (2008).
12. Krug, M. E., Dunand, D. C. & Seidman, D. N. Effects of Li additions on precipitation-strengthened Al–Sc and Al–Sc–Yb alloys. *Acta Mater.* **59,** 1700–1715 (2011).
13. Radmilovic, V., Tolley, A., Marquis, E. A., Rossell, M. D., Lee, Z. & Dahmen, U. Monodisperse $Al_3(LiScZr)$ core/shell precipitates in Al alloys. *Scr. Mater.* **58,** 529–532 (2008).
14. Hyland, R. W. Homogeneous nucleation kinetics of Al_3Sc in a dilute Al–Sc alloy. *Metall. Mater. Trans. A* **23,** 1947–1955 (1992).
15. Radmilovic, V., Fox, A. G. & Thomas, G. Spinodal decomposition of Al-rich Al–Li alloys. *Acta Metall.* **37,** 2385–2394 (1989).
16. Fox, A. G., Fuller, S. C., Radmilovic, V. & Whitman, C. A powder x-ray diffraction study of a solution treated and ice brine quenched Al–14.25 at.% Li alloy. *J. Mater. Res.* **6,** 712–718 (1991).
17. Yin, Y. & Alivisatos, A. P. Colloidal nanocrystal synthesis and the organic–inorganic interface. *Nature* **437,** 664–670 (2005).
18. Clouet, E., Barbu, A., Laé, L. & Martin, G. Precipitation kinetics of Al_3Zr and Al_3Sc in aluminum alloys modeled with cluster dynamics. *Acta Mater.* **53,** 2313–2325 (2005).
19. Robson, J. D. & Prangnell, P. B. Modelling Al_3Zr dispersoid precipitation in multicomponent aluminium alloys. *Mater. Sci. Eng. A* **352,** 240–250 (2003).
20. Tolley, A., Radmilovic, V. & Dahmen, U. Segregation in $Al_3(Sc, Zr)$ precipitates in Al–Sc–Zr alloys. *Scr. Mater.* **52,** 621–625 (2005).
21. Aydinol, M. K. & Bor, A. S. Coarsening of δ' (Al_3 Li) and composite precipitates in an Al-2.5-% Li-0.15-% Zr alloy. *J. Mater. Sci.* **29,** 15–25 (1994).
22. Kuehmann, C. J. & Voorhees, P. W. Ostwald ripening in ternary alloys. *Metall. Mater. Trans. A* **27,** 937–943 (1996).
23. Moreau, C., Allouche, A. & Knystautas, E. J. Measurements of the diffusion rate of lithium in aluminum at low-temperature by elastic recoil detection analysis. *J. Appl. Phys.* **58,** 4582–4586 (1985).
24. Fujikawa, S. I. Impurity diffusion of scandium in aluminium. *Defect Diffusion Forum* **143–147,** 115–120 (1997).
25. Royset, J. & Ryum, N. Kinetics and mechanisms of precipitation in an Al-0.2 wt.% Sc alloy. *Mater. Sci. Eng. A* **396,** 409–422 (2005).
26. Noble, B. & Bray, S. E. Use of the Gibbs–Thompson relation to obtain the interfacial energy of δ' precipitates in Al–Li alloys. *Mater. Sci. Eng. A* **266,** 80–85 (1999).
27. Murray, J. The Al–Sc system. *J. Phase Equilib.* **19,** 380–384 (1998).
28. Hallstedt, B. & Kim, O. Thermodynamic assessment of the Al–Li system. *Int. J. Mater. Res.* **98,** 961–969 (2007).
29. Mao, Z., Chen, W., Seidman, D. N. & Wolverton, C. First-principles study of the nucleation and stability of ordered precipitates in ternary Al–Sc–Li alloys. *Acta Mater.* **59,** 3012–3023 (2011).
30. Voorhees, P. W. & Johnson, W. C. Development of spatial correlations during diffusional late-stage phase transformations in stressed solids. *Phys. Rev. Lett.* **61,** 2225–2228 (1988).
31. LaMer, V. K. & Dinegar, R. H. Theory, production and mechanism of formation of monodispersed hydrosols. *J. Am. Chem. Soc.* **72,** 4847–4854 (1950).

32. Monachon, C., Dunand, D. C. & Seidman, D. N. Atomic-scale characterization of aluminum-based multishell nanoparticles created by solid-state synthesis. *Small* **6,** 1728–1731 (2010).

33. Perdew, J. P., Burke, K. & Ernzerhof, M. Generalized gradient approximation made simple. *Phys. Rev. Lett.* **77,** 3865–3868 (1996).

34. Blöchl, P. E. Projector augmented-wave method. *Phys. Rev. B* **50,** 17953–17979 (1994).

35. Kresse, G. & Joubert, D. From ultrasoft pseudopotentials to the projector augmented-wave method. *Phys. Rev. B* **59,** 1758–1775 (1999).

36. Kresse, G. & Hafner, J. *Ab-initio* molecular-dynamics for liquid-metals. *Phys. Rev. B* **47,** 558–561 (1993).

37. Kresse, G. & Hafner, J. *Ab-initio* molecular-dynamics simulation of the liquid-metal amorphous-semiconductor transition in germanium. *Phys. Rev. B* **49,** 14251–14269 (1994).

38. Kresse, G. & Furthmüller, J. Efficient iterative schemes for *ab initio* total-energy calculations using a plane-wave basis set. *Phys. Rev. B* **54,** 11169 (1996).

39. Van de Walle, A., Asta, M. & Ceder, G. M. The alloy theoretic automated toolkit: A user guide. *Calphad* **26,** 539–553 (2002).

Author contributions

V.R. conceived and designed the experiments and wrote the first draft of the manuscript. U.D., M.A. and C.O. co-wrote the manuscript. C.O. and M.A. performed first-principles simulation and continuum modelling. M.D.R. and V.R. carried out high-resolution microscopy and exit wave reconstruction. E.A.M. performed 3D-APT experiments and analysis. A.T., M.D.R. and A.G. carried out sample preparation and basic TEM characterization. V.R., U.D., M.A. and C.O. analysed the experimental results. All authors contributed to discussions.

Additional information

The authors declare no competing financial interests. Supplementary information accompanies this paper on www.nature.com/naturematerials. Reprints and permissions information is available online at http://www.nature.com/reprints. Correspondence and requests for materials should be addressed to V.R.